Soft Matter

PAPER

View Article Online
View Journal | View Issue

Cite this: *Soft Matter*, 2018, **14**, 7714

In-depth understanding of interfacial crystallization *via* Flash DSC and enhanced energy storage density in ferroelectric P(VDF-CTFE)/Au NRs nanocomposites for capacitor application†

Yingxin Chen, *[ad] Lingyun Yao,[a] Chengbiao Yang,[a] Lei Zhang,[a] Peng Zheng,[a] Aiping Liu*[b] and Qun-Dong Shen *[c]

High-capacity or high-power-density capacitors are being actively investigated for portable electronics, electric vehicles, and electric power systems. We describe the filler system in dielectric nanocomposites with a small loading of Au nanorods [NRs] to elucidate the mechanism of interfacial crystallization behavior including the crystallization kinetics, and crystalline morphology and structure, and to investigate the intrinsic causes for concurrent great improvements in the dielectric constant and energy density in the nanocomposite system. Remarkly, at high crystallization temperature, the addition of Au NRs, which are used as heterogeneous nucleators, can reduce the nucleation barrier, resulting in accelerating the crystallization rate. However, the crystallization rate slows down at low temperatures because the addition of Au NRs limited the mobility of poly(vinylidene fluoride-chlorotrifluoroethylene) [P(VDF-CTFE)] chains, and thus enhanced the diffusion barrier. Furthermore, the addition of NRs has a huge impact on the crystalline morphology and structure which changes from large paraelectric α-phase spherulites with TGTG′ conformations into minor ferroelectric γ-phase spherulites with T_3GT_3G' conformations, and also produces more exogenous interfaces between the lamellar crystals and amorphous regions, resulting in a higher dielectric constant and higher electric energy density in P(VDF-CTFE)/Au NRs nanocomposites. Our approach provides a facile and straightforward way to design or understand PVDF-based polymers for their practical applications in high-energy-density capacitors.

Received 22nd July 2018,
Accepted 23rd August 2018

DOI: 10.1039/c8sm01496e

rsc.li/soft-matter-journal

Introduction

Dielectric materials, which are used to be stored electric energy in the form of electrostatic charge, have been widely applied in various advanced electronic devices and power systems, such as large-scale energy storage grids, pulsed power systems and electronic components, and so on.[1–4] In the power supply system, a high-power-density capacitor is conducive to improving the environment of power supply and ensuring the stable operation of large electrical equipment.[1] Furthermore, the miniaturization of electronic products also requires to further reduce the volume of a large number of passive component capacitors on the circuit board.[5] Therefore, dramatic improvement of the energy density of capacitors would be essential to realize their full potential as an enabling technology.[6]

Poly(vinylidene fluoride) (PVDF) and its copolymers, which are serving as a new type of high dielectric matrix resin used for capacitive energy storage, have attracted wide scientific attention owing to their high storage density of electrical energy and high efficiency of electrical energy charging/discharging.[7–9] Nevertheless, to meet the requirements of practical high-capacity capacitors, PVDF-based copolymers such as poly(vinylidene fluoride-chlorotrifluoroethylene), *i.e.* P(VDF-CTFE), alone are barely enough.[10] After that, several methods have been used to modulate the crystalline structure and morphlology to improve the energy storage density of PVDF-based polymers themselves, such as grafting,[11,12] blending,[13,14] stretching,[15] electron irradiation,[16] and so on. Although these methods are effective to optimize one of the perfomances, the increase in energy storage capacity is limited or sacrificed. Remarkly, a nanocomposite approach with the addition of high-κ organic[17,18] and inorganic/ceramic particles[19–21] opens up a new avenue to design high-energy-density dielectric

[a] *College of Materials & Environmental Engineering, Hangzhou Dianzi University, Hangzhou, 310018, China. E-mail: yxchen@hdu.edu.cn*
[b] *Center for Optoelectronics Materials and Devices, Zhejiang Sci-Tech University, Hangzhou, 310018, China. E-mail: liuqiping1979@gmail.com*
[c] *Key Laboratory of High Performance Polymer Materials and Technology of MOE, School of Chemistry & Chemical Engineering, Nanjing University, Nanjing, 210023, China. E-mail: qdshen@nju.edu.cn*
[d] *Key Laboratory of Optoelectronic Chemical Materials and Devices, Ministry of Education, School of Chemical and Environmental Engineering, Jianghan University, Wuhan 430056, China*

† Electronic supplementary information (ESI) available. See DOI: 10.1039/c8sm01496e

materials, but also brings some new scientific problems, such as the compatibility between nanofillers and the matrix, interfacial polarization effects, the mechanism of crystallization kinetics at the interface, and how to regulate the crystalline structure and crystal morphology. Thus far, a great many efforts have focused on the issue of interfacial polarization effects[22,23] and the compatibility[24,25] between nanoparticles and the matrix. For example, Dang *et al.*[26] find that the TFP-MWNT/PVDF nanocomposite exhibits remarkably enhanced dielectric permittivity over the pristine PVDF polymer due to a remarkable Maxwell–Wagner–Sillars (MWS) effect. Furthermore, Nan *et al.*[27] found that $BaTiO_3$@TiO_2 nanofibers achieve concurrent enhancement of the electric displacement and breakdown strength in poly(vinylidene fluoride) (PVDF)-based nanocomposites due to greatly enhanced interfacial polarization. Nevertheless, there are relatively few studies that have focused on the mechanism of interfacial crystallization kinetics, and the ferroelecric/paraelectric crystal structure evolution in PVDF nanocomposites, which is critical to understand structure–property relationships to create PVDF-based nanocomposites with excellent energy storage capabilities.

Due to the fast crystallization ability of PVDF-based polymers, the very slow cooling and heating rates in conventional DSC cannot effectively track the crystallization kinetics and ferroelectric/paraelectric phase evolution at different annealing time and temperature, especially the effect of nanoparticles on the mechanism of interfacial crystallization kinetics. Recently, the fast cooling chip-calorimeter, *i.e.* flash differential scanning calorimeter,[28–31] with heating/cooling rates up to 5000 K s^{-1} has become an important tool in the study of non-isothermal and isothermal crystallization behaviors of polymers. Such a rapid cooling rate in Flash DSC allows precise control of the processing conditions, and offers a more detailed and useful way to study the effect of nanoparticles on the mechanism of interfacial crystallization and microstructure evolution, which will help us to understand and design PVDF nanocomposites.

In this paper, we present dielectric nanocomposites with a small loading of Au nanorods in a P(VDF-CTFE) matrix to elucidate the effect of the nanoparticles on the mechanism of crystallization kinetics, and the crystal morphology contributes to the extraordinary storage of electric energy in the dielectric polymer nanocomposites. For the first time, Flash DSC direct measurement of the crystallization rate of P(VDF-CTFE)/Au NRs nanocomposites was carried out and 3D profiles of enthalpy in the whole temperature range were measured, which is an extremely significant work on the mechanism of crystalline kinetics. Through this investigation, it is also intended to examine how the incorporation of Au NRs, which acted as heterogeneous nucleators, regulates the ferroelectric/paraelectric crystalline structure and crystal morphology in tandem with the corresponding electric storage behavior changes.

Experimental

Sample

P(VDF-CTFE) (91/9 mol%) was purchased from Solvay. Au nanorods (Au NRs) were purchased from Shanghai So–Fe Biomedicine Co., Ltd. The hexadecyltrimethylammonium bromide C_{16}TAB surfactant binds to the surface of gold nanorods.

Preparation of P(VDF-CTFE)/Au nanocomposites

0.14 g P(VDF-CTFE) was dissolved in *N*,*N*-dimethylformamide at room temperature. 0, 280 or 980 μl Au NRs was added into the solution to obtain 0 wt%, 0.02 wt%, and 0.07 wt% P(VDF-CTFE)/Au nanocomposites (NCs), which were named as N_0, N_1, and N_2, respectively. The solutions were treated under ultrasound for 0.5 h for making homogeneous dispersions. The final solutions were cast on glass plates and dried at 60 °C in an air-circulation oven for 72 h, and finally in a vacuum oven for 24 h to remove residual solvent. Furthermore, the samples were firstly hot-pressed at 220 °C, and then were annealed at 140 °C for 1 hour, and finally cooled down to room temperature. The resultant thickness of the films was about 30–40 μm.

Sample characterization

Morphology characterization

The morphology of Au nanorods was examined by transmission electron microscopy (TEM, JEM-2100); atomic force microscopy (AFM) images of nanocomposites N_0, N_1, and N_2 were captured on a Dimension Icon Scan Asyst atomic force microscope (Bruker Co.). Before scanning, the films annealed at 140 °C for 1 h.

Crystallization behavior characterization

A polarized optical microscope (POM, Olympus BX51-P) with a hot stage unit was used to study the spherulite morphologies of P(VDF-CTFE) and P(VDF-CTFE)/Au nanocomposites N_1 and N_2. All the samples were first heated to 240 °C at 10 °C min^{-1} and subsequently cooled down to 140 °C for different annealing time.

Flash differential scanning calorimeter, (Flash DSC) was performed by using a commercially available chip-calorimeter (Flash DSC1, Mettler-Toledo Co.) with a mechanical-intercooler and nitrogen purge gas. The calorimetric chip-sensor was conditioned five times and corrected one time according to the standard procedure prior to use. The samples were cut into small pieces (about 100 nanogram) and then were transferred to the sensor center within an area of 0.2–0.5 $mm.^2$

Dielectric and energy storage characterization

The dielectric properties were determined as a function of frequency from 100 to 10^6 Hz *via* a high-precision LCR meter (HP4284A; Agilent, Palo Alto, CA) at a bias voltage of 1 V. The bipolar and unipolar *D–E* loops were acquired by using a Radiant Technologies Precision Premier II equipped with a TREK model 2210 amplifier with the maximum voltage of 10 000 V at a frequency of 10 Hz. Gold electrodes 60 nm thick were sputtered on both surfaces of the polymer films for electric measurements. The gold electrode area was *ca.* 0.19625 cm^2 for the *D–E* loop measurements. Stored and released energy densities (U_e) were obtained by integrating the corresponding charging and discharging curves, $U = \int E\mathrm{d}D$.

Structure characterization

The crystalline structures of P(VDF-CTFE) and nanocomposites N_1 and N_2 were studied using a Fourier transform infrared spectroscopy (FTIR, Bruker Tensor) instrument and an X-ray diffractometer (XRD, Bruker-D8). The XRD data was collected from 2θ = 5–30° at a scanning speed of 2° min^{-1} with a step interval of 0.02°. The instrument was operated at a 35 kV voltage and 30 mA current. FTIR spectra were recorded at a resolution of 2 cm^{-1} and 32 scans from 4000 cm^{-1} to 400 cm^{-1} were averaged.

Results and discussion

Preparation of P(VDF-CTFE)/Au NRs nanocomposites

We present and demonstrate a new design of the filler system in dielectric polymer nanocomposites for changing the microstructure (crystalline unit cell, chain conformation and semicrystalline morphology) and in turn the electrical charge storage capability under a weak electric field of the nanocomposites, where Au nanorods are chosen as the nanofillers, and P(VDF-CTFE) is a promising high-energy-density dielectric material for capacitors, and thus is selected as the matrix. In Fig. 1a, it is obvious from the TEM image that Au nanorods are cylindrical with uniform sizes. The distribution of the diameter and length of Au nanorods in Fig. 1a was calculated by the soft ''nano measurer'' and shown in Fig. S1 (ESI†). The mean diameter and length of Au nanorods are about 27.9 nm and 104 nm, respectively. P(VDF-CTFE)/Au NRs nanocomposites are fabricated by very simple blending of the Au nanorods and the copolymer solution, followed by a solution-cast procedure to afford uniform and flexible films, as shown in Fig. 1b. AFM phase imaging of nanocomposite films with 0, 0.02, and 0.07 wt% of Au NRs is measured by atomic force microscopy, as shown in Fig. 1c–e. The Au NRs are well separated and uniformly embedded in the P(VDF-CTFE) matrix. With the increase of Au NRs content, more Au NRs are observed on the surface of nanocomposite N_2. Herein, nanofillers were used as a means of enhancing polar phase crystal formation and scaling down the spherulite size in P(VDF-CTFE). Two different types of interface are built in the P(VDF-CTFE) nanocomposites. One is the new interface between Au nanorods and the P(VDF-CTFE) matrix, and the other is the interface between the crystalline phase and the amorphous phase.[21,32]

Crystallization behaviour

In comparison to conventional DSC, Flash DSC with rapid cooling and heating rates overcomes the shortcoming that conventional DSC cannot effectively track the crystallization behavior of the fast-crystallization PVDF-based polymers, and then offers a more detailed and useful way to study the microstructure evolution of P(VDF-CTFE) and nanocomposites in the full temperature range. Temperature programs of our isothermal measurements are depicted in Fig. 2a. The sample was firstly melted at 240 °C for 60 s to erase its thermal history and then was cooled to a crystallization temperature for a certain period up to 6400 s before quenching and heating scans at fixed cooling and heating rates of 5000, and 1000 K s^{-1}, respectively.

The heating curves of apparent heat capacities of P(VDF-CTFE)/Au NRs nanocomposites N_1 and N_2 prepared with various annealing times at a crystallization temperature of 140 °C are summarized in Fig. 2b and c. When the annealing time is below 800 s, a crystallization peak of nanocomposite N_1 appears at 110–140 °C. With increasing the annealing time above 800 s, a new high-temperature peak at 165 °C can be seen and its

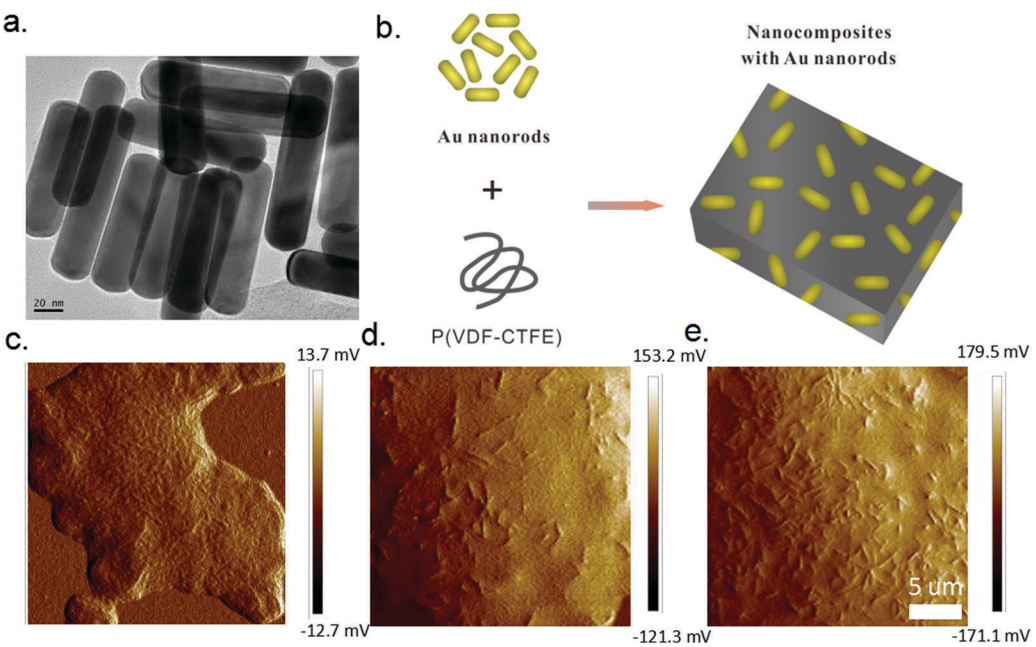

Fig. 1 (a) TEM image of the monodisperse Au nanorods, (b) illustration of the process for fabrication of the nanocomposites, and AFM phase imaging of P(VDF-CTFE)/Au nanocomposites: (c) pristine P(VDF-CTFE) N_0, (d) N_1, and (e) N_2 annealed at 140 °C for 1 h; the scale bar is 5 μm.

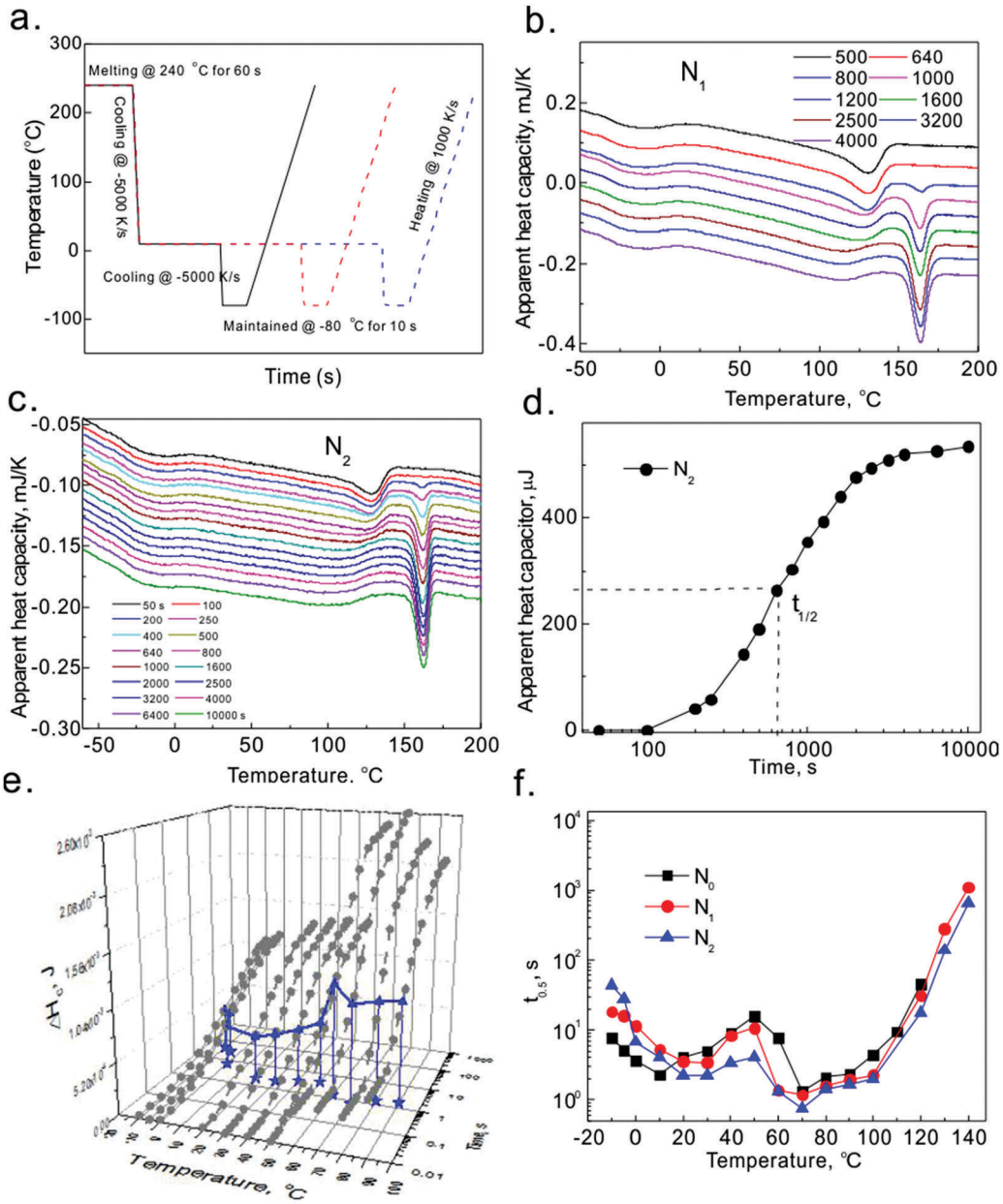

Fig. 2 (a) Temperature–time profiles of fast-scan measurements. The samples were prepared by the cooling rate −5000 K s^{-1} at the selected temperature for various time durations up to 6400 s; (b and c) heating curves of heat capacities of nanocomposites N_1 and N_2 after annealing at various time durations at the selected temperature T_x = 140 °C. (d) Logarithmic time–enthalpy curves of isothermal crystallization estimate the crystallization half-time (the *x*-axis represents the annealing time and each point comes from an independent experiment) at the crystallization temperature 140 °C. (e) 3D profiles of the enthalpy curve dependence on varying crystallization temperature and time for P(VDF-CTFE)/Au NRs nanocomposite N_2. Among them, the crystallization half-time $t_{1/2}$ in 3D profiles was marked by the triangle point at different annealing temperature and *X*–*Y* projection point was labeled out by the pentagram on the *X*–*Y* plane. (f) Isothermal crystallization half-time of N_0, N_1 and N_2 as a function of temperature.

intensity grows, suggesting that the high temperature peaks must be heterogeneous crystals formed during annealing at 140 °C. By contrast, the time required for nucleation is approximately 200 s, faster than that of N_1, in agreement with measurements of nucleation rates performed by POM, as shown in Fig. 2c. At a crystallization temperature of 140 °C, a time–enthalpy curve of isothermal crystallization of nanocomposites N_1 and N_2 is shown in Fig. 2d and its crystallization half-time ($t_{1/2}$) can be obtained in the time window of our observation. The obtained crystallization half-time ($t_{1/2}$) of N_2 is about 645 s. Moreover, the 3D profile of the enthalpy of N_2, which is closely related to the crystal size, is dependent on the full crystallization temperature and time, as shown in Fig. 2e. The crystallization half-time $t_{1/2}$, which is an expression of the overall crystallization rate, is plotted as a function of isothermal crystallization temperatures, and the *X*–*Y* projection of $t_{1/2}$ is depicted clearly in Fig. 2e. The comparison of the crystallization half-time of nanocomposites N_0, N_1, and N_2 is depicted in Fig. 2f. It is

observed that P(VDF-CTFE)/Au NRs nanocomposites (N_0, N_1 and N_2) show two inverse bell-shaped curves of overall crystallization half-time (inversely proportional to the overall crystallization rate) which can be explained by the classical theory of nucleation and growth. The following Turnbull–Fisher equation has been utilized to analyze the details of this phenomenon.[33] Two minima were observed. One minimum at high temperature is related to the fast growth rate of heterogeneous crystal nucleation, and the other one at low temperature corresponds to the fast growth rate of homogenous crystal nucleation. The sample annealed at low temperature below 50 °C forms the homogenous crystal between neighboring primary crystals due to homogeneous nucleation, while the sample annealed at high temperature above 50 °C forms the primary α/γ crystal due to the heterogeneous nucleation. Interestingly, the addition of Au NRs in the P(VDF-CTFE) copolymers shows significant differences in the crystallization half-times. For the high-temperature process, the crystallization rate of the filled material is obviously accelerated with the increase in the content of Au nanorods. For example, at a high crystallization temperature of 140 °C, the crystallization half-time of N_2, which is about 645 s, is 1.7 times faster than that of N_1. However, for the low-temperature process between −3 and 20 °C, the crystallization half-time prolongs and the crystallization rate of nanocomposites slows down because the existence of Au NRs is not beneficial to form the tiny crystal from adjacent molecular chains. However, the crystallization of N_2 is still faster than that of N_1. Subsequently, when the crystallization temperature is below −3 °C, the crystallization rate of N_2 further slows down, and is the slowest in the three samples.

According to the classical crystallization theory of polymers,[34] we can characterize the crystallization half-time, $t_{1/2}$, by a diffusion barrier, E_a (the apparent activation energy of molecular transport to the growth face of the crystals), and the nucleation barrier, ΔG (the work required for formation of nuclei), as shown in eqn (1).

$$t_{1/2} \propto \exp\left(\frac{E_a}{RT} + \frac{\Delta G}{RT}\right) \quad (1)$$

where R is the gas constant and T is the temperature. In high temperatures, the nucleation barrier controls the crystallization process. The addition of Au NRs, which are used as heterogeneous nucleators, leads to reducing the nucleation barrier, and then accelerates the crystallization rate. Similar results are observed in the POM experiments. At low temperatures, the crystallization process is mainly controlled by the diffusion barrier.[40] The addition of Au NRs limited the mobility of P(VDF-CTFE) chains and then enhanced the diffusion barrier. Therefore, the crystallization rate of the P(VDF-CTFE)/Au NRs nanocomposite slows down.

Crystalline morphology

Fig. 3 shows the POM images of pristine P(VDF-CTFE) and the P(VDF-CTFE)/Au nanocomposite crystallized at 140 °C for different annealing times from the melt. In Fig. 3a, one type of spherulite with high birefringence and closely spaced concentric banding is seen in the pristine P(VDF-CTFE). The spherulites are the typical

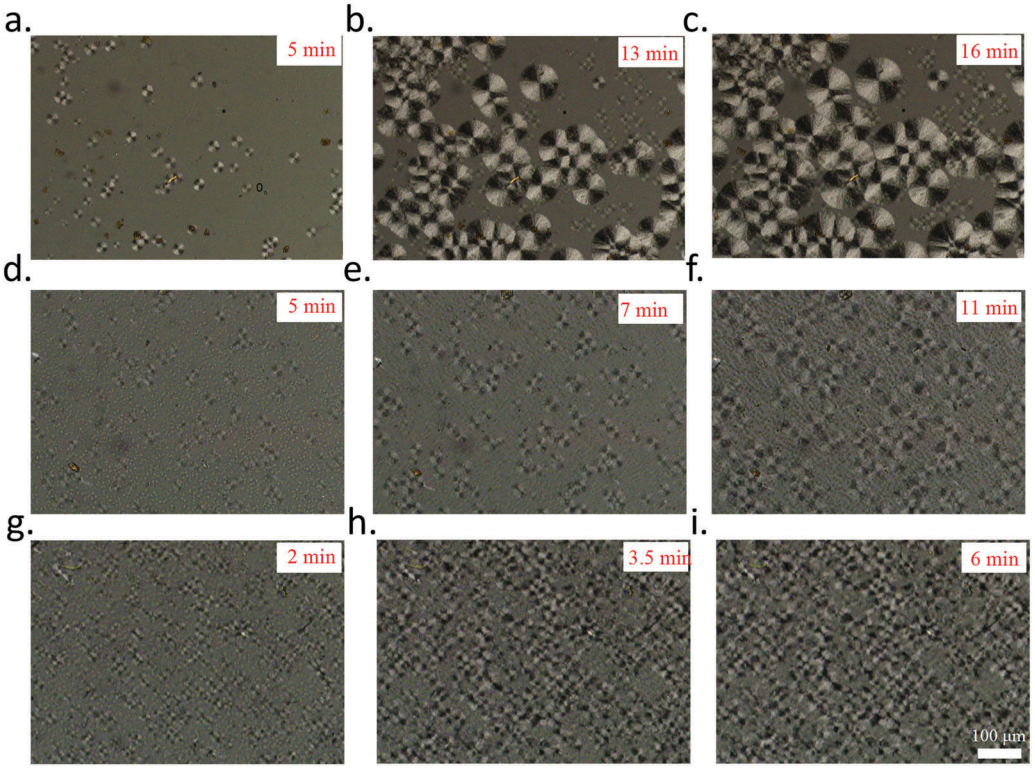

Fig. 3 POM images of the spherulites crystallized at 140 °C dependence on time (a) 5 min, (b) 13 min, and (c) 16 min for neat P(VDF-CTFE); (d) 5 min, (e) 7 min, and (f) 11 min for nanocomposite N_1; and (g) 2 min, (h) 3.5 min, and (i) 6 min for nanocomposite N_2; with scale bars of 100 mm.

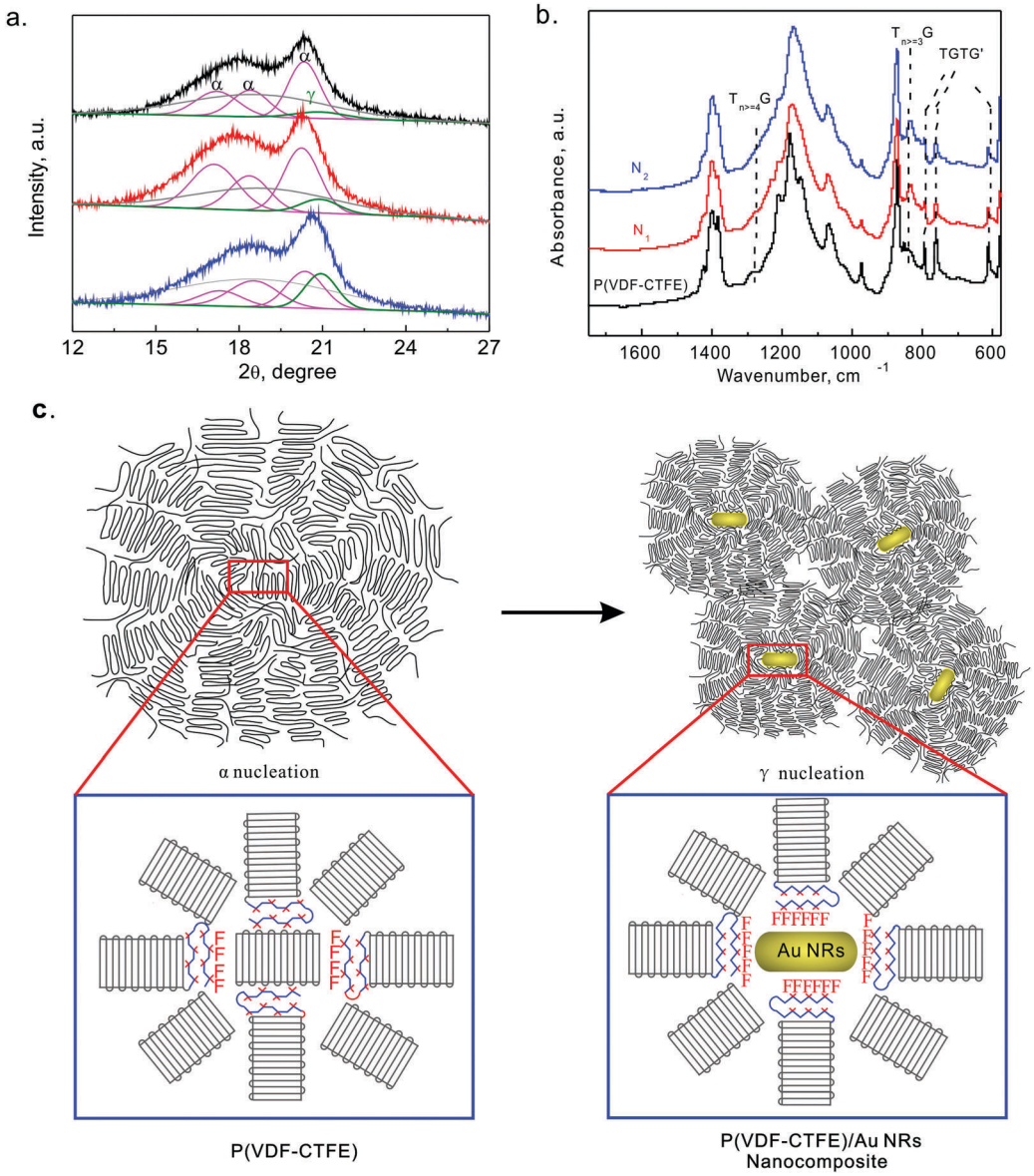

Fig. 4 (a) Room-temperature X-ray diffraction patterns of pristine P(VDF-CTFE), and nanocomposites N_1 and N_2, and the curve is well fitted by Gaussians. (b) FTIR spectra of pristine P(VDF-CTFE), N_1 and N_2. (c) The schematic diagram of the nucleation mechanism of the spherulites in P(VDF-CTFE) and the composite system with Au NRs.

paraelectric crystals.[35,36] With addition of Au nanorods, darker and less birefringent spherulites of the ferroelectric phase appear in addition to the bright and highly birefringent spherulites of the paraelectric phase,[35,37] and the content of ferroelectric crystals increases with the increase of Au nanorods. Moreover, the addition of Au nanorods, which served as heterogeneous nucleators, accelerates the crystallization rate of P(VDF-CTFE), and scales down the size of the spherulite. It results in producing more interfaces between the crystalline phase and amorphous phase. Based on all the above discussions, it is expected to enhance the capacity of charge storage when applying an electric field through metal electrodes on both sides of the specimens, where the charges will be preferably stored at the nanoparticle/matrix interfaces and crystalline/amorphous interfaces.

Crystalline structure

We performed further characterization of the polymorphic crystalline phases of P(VDF-CTFE)/Au NRs nanocomposites, by using WAXD and FTIR, as summarized in Fig. 4a and b. The P(VDF-CTFE) sample exhibits three peaks at 17.2°, 18.2°, and 20.3°, which can be assigned to (100), (020), and (110) reflections of the nonpolar crystalline α-phase similar to PVDF, respectively. Its intensity decreases with the increase of Au NRs. By contrast, a diffraction peak around 20.8° (the interplanar spacing d = 4.25 Å) is ascribed to the β/γ-phase of VDF sequences. Its intensity grows with the increase in the content of Au NRs. In Fig. 4b, the bands at 841 cm^{-1}, which belong to $T_{n\geq 3}G$ conformations in the crystalline γ-phase, increase remarkably in intensity with the increase in the content of Au NRs, while the

Table 1 Lattice constant and coherence length for the (200, 020) reflection of P(VDF-CTFE)/Au NR nanocomposites (N_0, N_1 and N_2)

	γ-Phase		α-Phase	
	d, Å (200)	L, nm	d, Å (020)	L, nm
N_0	4.25	3.7	4.86	6.1
N_1	4.25	5.0	4.83	5.3
N_2	4.26	5.4	4.81	4.0

absorbances at 768 and 614 cm^{-1} for the TGTG′ conformation in the crystalline α-phase decrease in turn.

Furthermore, the structural data of P(VDF-CTFE)/Au NRs nanocomposites (N_0, N_1 and N_2) are summarized in Table 1. The crystallite sizes or coherence lengths (L) perpendicular to the crystallographic plane,[38,39] corresponding to the sizes of the α-phase or β/γ-phase, are estimated using the Scherrer eqn (2):

$$L = \frac{0.9\lambda}{B\cos\theta} \quad (2)$$

where λ is the X-ray wavelength and B and θ are the full width at half maximum (in 2θ) and angular position of the diffraction peaks, respectively. The paraelectric crystallite size of pristine P(VDF-CTFE) is 6.1 nm, larger than that of the P(VDF-CTFE)/Au NRs nanocomposites (N_1: 5.3 nm, N_2: 4.0 nm). It is reasonable that Au NRs served as heterogeneous nucleators and lead to reducing the nucleation barrier. It is beneficial to form the tiny spherulites on the surface of Au NRs. On the contrary, the ferroelectric γ crystalline size grows from 3.7 to 5.4 nm with the increase of Au NRs content, as shown in Table 1. This phenomenon also suggests that the conformational transition from the paraelectric α-phase to ferroelectric γ-phase was induced by Au NRs doping.

Compared to pure P(VDF-CTFE), the Au NRs, a nucleating agent, are very effective in promoting heterogeneous nucleation of P(VDF-CTFE), leading to accelerating the crystallization rate of the composite system. Meanwhile, the addition of Au NRs has a huge effect on the crystalline properties of the composite system, such as the size of the spherulite and chain conformation. In Fig. 4c, pure P(VDF-CTFE) shows a tendency to form large paraelectric α-phase spherulites with TGTG conformations which stem from the close-packed grains nucleated by self-nucleation processes. However, the composite system tends to grow into minor ferroelectric γ-phase spherulites with T_3GT_3G' conformations.

Bipolar *D–E* curves

Fig. 5 compares bipolar *D–E* hysteresis loops of nanocomposites, including the pristine P(VDF-CTFE), and P(VDF-CTFE)/Au NRs nanocomposites (N_1 and N_2). A sinusoidal ac electric field (100 Hz) was applied across the polymer film with an initial amplitude of 20 MV m^{-1}, then increasing in 20 MV m^{-1} intervals until reaching the breakdown electric field. In Fig. 5a–c, pristine P(VDF-CTFE) and the composite systems (N_1 and N_2) show

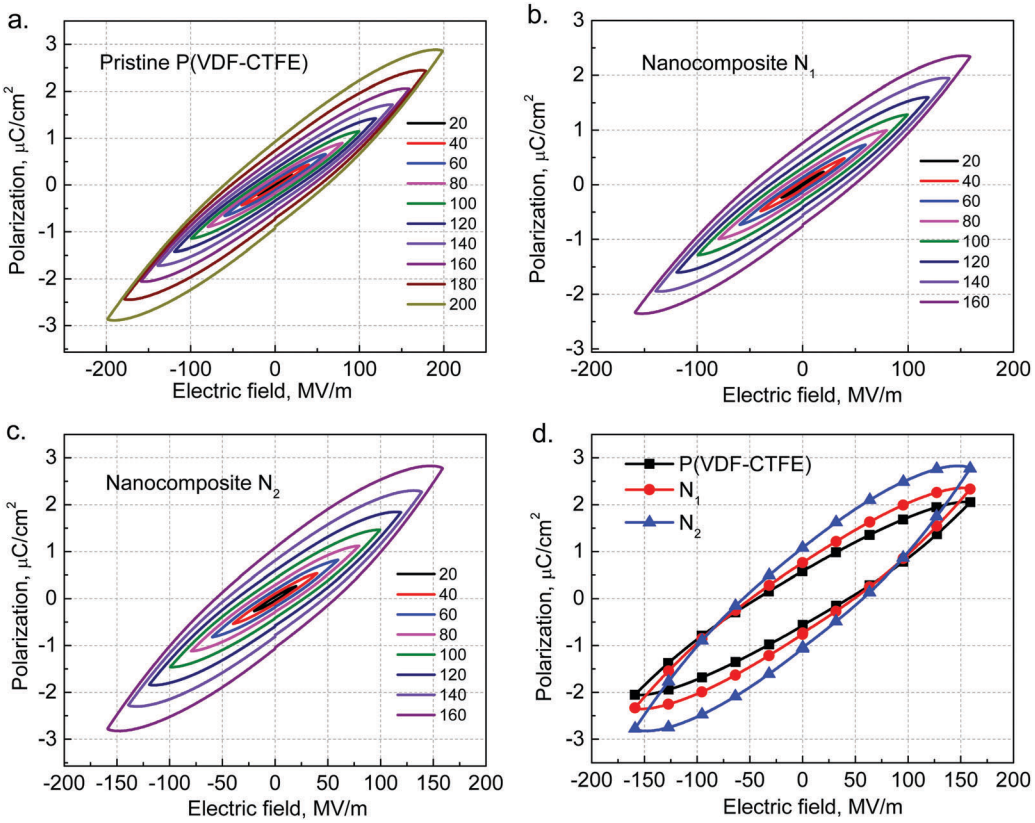

Fig. 5 Bipolar *D–E* hysteresis loops of (a) pristine P(VDF-CTFE); (b) N_1; and (c) N_2; and (d) comparison of bipolar *D–E* hysteresis loops under E = 160 MV m^{-1} for the pristine, and P(VDF-CTFE)/Au NRs nanocomposites (N_1 and N_2).

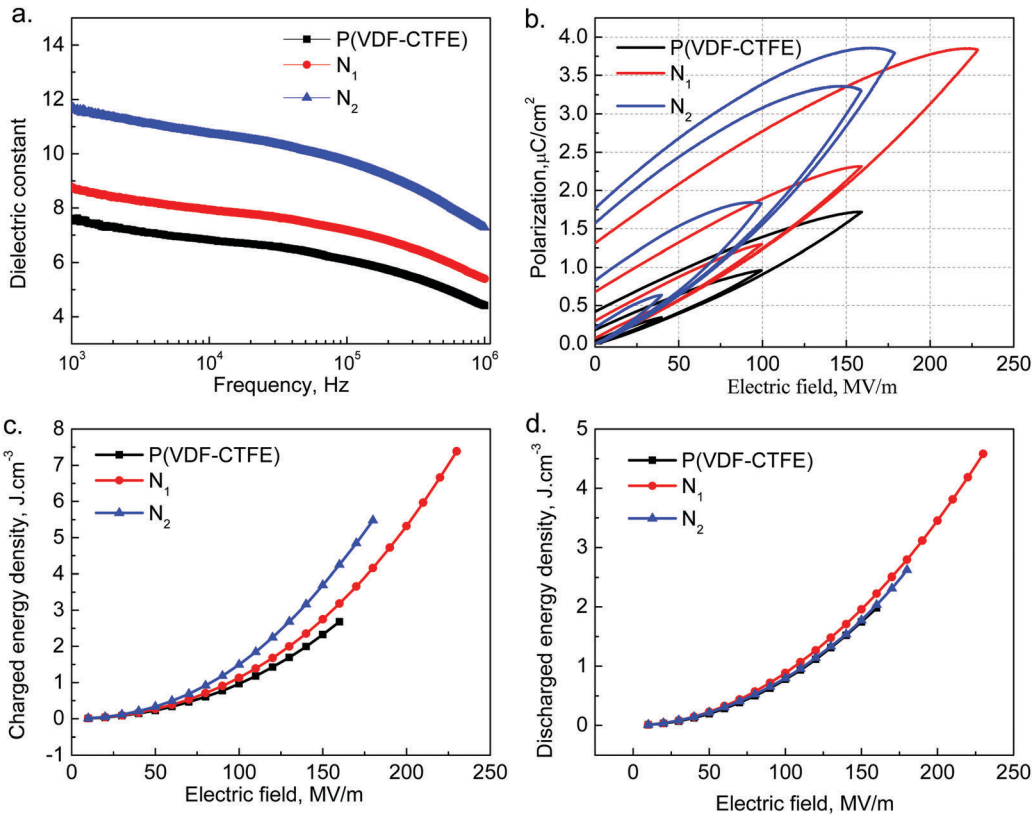

Fig. 6 Frequency dependence of the relative permittivity of pristine P(VDF-CTFE), and P(VDF-CTFE)/Au NR nanocomposites N_1 and N_2 measured at room temperature from 0.5 kHz to 1 MHz. (b) Unipolar *D*–*E* hysteresis loops, (c) charged energy density and (d) discharged energy density of pristine P(VDF-CTFE), and P(VDF-CTFE)/Au NRs nanocomposites N_1 and N_2 as a function of the field strength.

similar *D*–*E* hysteresis loops, and the remnant polarization (the polarization level at $E = 0$ in the hysteresis loop) and the coercive field (the field level at $P = 0$ in the hysteresis loop) gradually enlarge with the increasing field amplitude. The pristine P(VDF-TrFE) film measured at room temperature exhibits a typical paraelectric polarization hysteresis loop (Fig. 5a) with a coercive field E_c of 60.1 MV m^{-1} and a remnant polarization P_r of 2.9 μC cm^{-2} at an electric field of 200 MV m^{-1}. In contrast, the composite system exhibits a slight polarization hysteresis loop, resulting from slowly increasing the remnant polarization, coercive field, and the saturation polarization P_s with the increasing content of Au NRs. In Fig. 5d, at the same electric field of 160 MV m^{-1}, P_r, E_c, and P_s values of pristine P(VDF-CTFE) are 0.59, 43.9 MV m^{-1}, and 2.0 μC cm^{-2}, respectively, and the values of nanocomposite N_2 are up to 1.1 μC cm^{-2}, 57.4 MV m^{-1}, and 2.8 μC cm^{-2}, respectively. The intrinsic cause for improved ferroelectric properties may be mainly correlated with some changes of crystalline morphology and structure which change large paraelectric α-phase spherulites to minor ferroelectric γ-phase spherulites.

Dielectric and energy storage and release behavior

P(VDF-CTFE) copolymers have also been shown to generate large electric polarization, high energy density, and rapid polarization switching, which are utilized as an energy storage capacitor. According to the above discussions, the addition of heterogeneous nucleators Au NRs has a great effect on the crystalline morphology and structure, resulting in good ferroelectric behavior. Herein, in order to develop high-energy-density dielectric materials for capacitor applications, further in-depth research of dielectric and energy storage/release behavior is necessary. The effects of Au NRs on the dielectric properties of P(VDF-CTFE) are presented in Fig. 6a. At the testing frequency of 1 kHz, the dielectric constant of the composite systems raised from 7.3 to 11.7 with the increase in the content of Au NRs from 0 wt% to 0.7 wt%. It is known to all that the relative dielectric constant mostly reflects the mobility of the dipole moments in the amorphous phase and small crystal domains at low electric fields. Accordingly, the explanation for the improved dielectric constant of the composite system has three reasons. Firstly, a small spherulite size is formed in the composite system (Fig. 2), and thus more charges are built up at the interfaces between the crystalline and amorphous phase to afford a high dielectric constant. Secondly, the response of the dipole moment of γ-phase spherulites in the composite system is higher than that of α-phase spherulites in pure P(VDF-CTFE). Thirdly, the high specific surface areas bring enormous interfaces at the boundary of Au NRs. The results suggest that these key dielectric characteristics could be readily customized to suit capacitor application by simply tailoring the composite compositions.

Furthermore, typical unipolar *D*–*E* responses, where *E* is the electric field and *D* is the electric displacement, measured at various mass fractions of Au NRs are presented in Fig. 6b. With the gradual increase of the field strength, the electric displacement of

P(VDF-CTFE) increases and reaches the maximum, which is defined as the charging process of electric energy in the capacitor. Then, while the electric field is steadily reduced, the electric displacement decreases leading to electric energy discharging from the copolymer, which is named as the discharging process. Hence, the charged and discharged energy density can be directly calculated from unipolar *D–E* loops by the integral $U = \int E\mathrm{d}D$, as shown in Fig. 6c and d. Typical *D–E* loops presented in Fig. 6b indicate clearly a concurrent and marked increase in both *D* and breakdown field E_b from pristine P(VDF-CTFE) to the nanocomposite system, which are consistent with the dielectric spectroscopic and bipolar *D–E* curves. Under the same field amplitudes, the electric displacement of the nanocomposites increases with the increasing content of Au NRs. At the same electric field of 160 MV m^{-1}, pristine P(VDF-CTFE) (N_0) exhibits a relatively low level of electric displacement of about 1.7 μC cm^{-2}, while the value of N_1 and N_2 reaches 2.3 and 3.3 μC cm^{-2}, respectively. The enhancement of the electric displacement value may be closely related to the fact that the addition of Au NRs is helpful to form a tiny spherulite size with the γ-phase in P(VDF-CTFE)/Au NRs nanocomposites, as proved by the above POM, XRD and FTIR results. Consequently, the nanocomposite system shows more improved values of charged energy density and discharged energy density with respect to pristine P(VDF-CTFE). For instance, the charged and discharged energy densities of N_0 are about 2.7 and 2.0 J cm^{-3} at the maximum electric field of 260 MV m^{-1}, and those of N_2 are 7.4 and 4.6 J cm^{-3} at the maximum electric field of 230 MV m^{-1}. In a word, the spherulite sizes are reduced with the addition of Au NR fillers. The existence of small spherulites coupled with a γ-phase facilitates dipole orientation to achieve high discharged energy density during the charging and discharging process. The excellent performance, which is attained by a small loading of the nucleators, makes the nanocomposite system a promising candidate for compact and flexible high-energy high-power capacitive energy storage devices.

Conclusions

In this article, we have prepared P(VDF-CTFE)/Au NRs nanocomposites by adding a small fraction of Au nanorods for high-capacity electric energy storage purposes. By means of both fast-scan DSC measurements and POM observations, we systematically study how Au NRs act as nucleating agents to modify the crystallization behavior of P(VDF-CTFE), their related microstructures and in turn the electrical energy storage characteristics of the P(VDF-CTFE) copolymer. From the viewpoint of crystallography, a bimodal distribution of the crystallization rate of P(VDF-CTFE)/Au NR nanocomposites (N_0, N_1, and N_2) in the whole temperature range is revealed by Flash DSC. Interestingly, at high temperatures, the addition of Au NRs, which are used as heterogeneous nucleators, leads to reducing the nucleation barrier, and then accelerates the crystallization rate. At low temperatures, the addition of Au NRs limited the mobility of P(VDF-CTFE) chains, and then improved the diffusion barrier, leading to a reduced crystallization rate of P(VDF-CTFE)/Au NR nanocomposites. Meanwhile, the addition of Au NRs has a huge effect on the crystalline properties of the composite system, such as the size of the spherulite and chain conformation. Pure P(VDF-CTFE) shows a tendency to form large paraelectric α-phase spherulites with TGTG conformations which stem from the close-packed grains nucleated by self-nucleation processes. However, the composite system tends to grow into minor ferroelectric γ-phase spherulites with T_3GT_3G' conformations because Au NRs can act as heterogenous nuclei.

From the viewpoint of dielectric and electric energy storage, the enhancement of the dielectric constant observed in P(VDF-CTFE)/Au NR nanocomposites was mainly attributed to strong interfacial polarization which stems from more interfaces between crystalline and amorphous phases by heterogeneous nucleation. Secondly, the improvement of the charge/discharge energy density of P(VDF-CTFE)/Au NRs nanocomposites may be closely related to the fact that incorporation of Au NRs leads to ferroelectric polar crystals with a concomitant decrease of the spherulite size, which facilitates dipole orientation to achieve high discharged energy density during the charging and discharging process. Our systematic observations facilitate a better understanding of crystallization behavior and structural optimization to design PVDF-based polymers for their real applications in high-capacitance and efficient capacitors.

Conflicts of interest

There are no conflicts to declare.

Acknowledgements

This work was supported by National Natural Science Foundation of China (Grant No. 51703044), the School Science Starting Foundation of Hangzhou Dianzi University (Grant No. KYS205617016), College of Science and Technology Innovation Program (Xinmiao plan) of Zhejiang province (No. 2017R407035), Natural Science Foundation of Jiangsu Province (No. BK20171336), and the Opening Project of Key Laboratory of Optoelectronic Chemical Materials and Devices, Ministry of Education, Jianghan University (No. JDGD-201804). We are grateful for helpful discussions and testing platform of Flash measurements offered by Prof. Wenbing Hu at Nanjing University.

References

1 B. J. Chu, X. Zhou, K. L. Ren, B. Neese, M. R. Lin, Q. Wang, F. Bauer and Q. M. Zhang, *Science*, 2006, **313**, 334–336.
2 Z.-M. Dang, M.-S. Zheng and J.-W. Zha, *Small*, 2016, **12**, 1688–1701.
3 Y. Feng, B. Miao, H. Gong, Y. Xie, X. Wei and Z. Zhang, *ACS Appl. Mater. Interfaces*, 2016, **8**, 19054–19065.
4 X. Huang and P. Jiang, *Adv. Mater.*, 2015, **27**, 546–554.
5 H. G. Wisken and T. H. G. G. Weise, *IEEE Trans. Magn.*, 2003, **39**, 501–504.
6 W. J. Sarjeant, J. Zirnheld, F. W. MacDougall, J. S. Bowers, N. Clark, I. W. Clelland, R. A. Price, M. Hudis, I. Kohlberg,

G. McDuff, I. McNab, S. G. Parler Jr and J. Prymak, *Handbook of Low and High Dielectric Constant Materials and Their Applications*, Academic Press, Burlington, 1999.
7 C. Yang, P. C. Irwin and K. Younsi, *IEEE Trans. Dielectr. Electr. Insul.*, 2004, **11**, 797–807.
8 M. Rabuffi and G. Picci, *IEEE Trans. Plasma Sci.*, 2002, **30**, 1939–1942.
9 L. A. Fredin, Z. Li, M. A. Ratner, M. T. Lanagan and T. J. Marks, *Adv. Mater.*, 2012, **24**, 5946–5953.
10 X. Zhou, B. Chu, B. Neese, M. Lin and Q. M. Zhang, *IEEE Trans. Dielectr. Electr. Insul.*, 2007, **14**, 1133–1138.
11 Y. F. Zhao, Q. Li, X. Zhang, H. Y. Li, J. Y. Lu and Z. C. Zhang, *Macromol. Chem. Phys.*, 2018, **219**, 1700621.
12 S. Tan, J. Li, G. X. Gao, H. Y. Li and Z. C. Zhang, *J. Mater. Chem.*, 2012, **22**, 18496–18504.
13 X. D. Zhao, J. Zhao, J. P. Cao, X. Y. Wang, M. Chen and Z. M. Dang, *J. Phys. Chem. B*, 2013, **117**, 2505–2515.
14 M. S. Zheng, J. W. Zha, Y. Yang, P. Han, C. H. Hu, Y. Q. Wen and Z. M. Dang, *Appl. Phys. Lett.*, 2017, **110**, 252902.
15 H. H. Gong, B. Miao, X. Zhang, J. Y. Lu and Z. C. Zhang, *RSC Adv.*, 2016, **6**, 1589–1599.
16 B. Vivek, Z. Xia and Q. M. Zhang, *Science*, 1998, **280**, 2101–2104.
17 Q. Li, K. Han, M. R. Gadinski, G. Z. Zhang and Q. Wang, *Adv. Mater.*, 2014, **26**, 6244–6249.
18 J. W. Wang, Q. D. Shen, H. M. Bao, C. Z. Yang and Q. M. Zhang, *Macromolecules*, 2005, **38**, 2247–2252.
19 K. Yu, H. Wang, Y. C. Zhou, Y. Y. Bai and Y. J. Niu, *J. Appl. Phys.*, 2013, **113**, 034105.
20 P. H. Hu, Y. Song, H. Y. Liu, Y. Shen, Y. H. Lin and C. W. Nan, *J. Mater. Chem. A*, 2013, **1**, 1688–1693.
21 Y. Chen, X. Tang, J. Shu, X. Wang, W. Hu and Q.-D. Shen, *J. Polym. Sci., Part B: Polym. Phys.*, 2016, **54**, 1160–1169.
22 B.-H. Fan, J.-W. Zha, D. Wang, J. Zhao and Z.-M. Dang, *Appl. Phys. Lett.*, 2012, **100**, 012903.
23 B. Chu, M. Lin, B. Neese, X. Zhou, Q. Chen and Q. M. Zhang, *Appl. Phys. Lett.*, 2007, **91**, 122909.
24 J. Guan, C. Xing, Y. Wang, Y. Li and J. Li, *Compos. Sci. Technol.*, 2017, **138**, 98–105.
25 C. Xing, L. Zhao, J. You, W. Dong, X. Cao and Y. Li, *J. Phys. Chem. B*, 2012, **116**, 8312–8320.
26 Z. M. Dang, L. Wang, Y. Yin, Q. Zhang and Q. Q. Lei, *Adv. Mater.*, 2007, **19**, 852–857.
27 X. Zhang, Y. Shen, Q. Zhang, L. Gu, Y. Hu, J. Du, Y. Lin and C.-W. Nan, *Adv. Mater.*, 2015, **27**, 819–824.
28 Y.-X. Chen, H.-W. Lu, Z.-W. Shen, Z.-L. Li and Q.-D. Shen, *J. Polym. Sci., Part B: Polym. Phys.*, 2017, **55**, 1245–1253.
29 Y. X. Chen, X. Chen, D. S. Zhou, Q.-D. Shen and W. B. Hu, *Polymer*, 2016, **84**, 319–327.
30 J. Wang, Z. Li, R. A. Pérez, A. J. Müller, B. Zhang, S. M. Grayson and W. Hu, *Polymer*, 2015, **63**, 34–40.
31 H. Gao, J. Wang, C. Schick, A. Toda, D. Zhou and W. Hu, *Polymer*, 2014, **55**, 4307–4312.
32 X. Z. Chen, Z. X. Cheng, L. Liu, Q. D. Shen and W. B. Hu, *Colloid Polym. Sci.*, 2013, **291**, 1989–1997.
33 E. Schulz and B. Wunderlich, *Macromolecular physics, Vol. 2 crystal nucleation, growth, annealing*, Academic, New York, 1976, p. 50.
34 J. E. K. Schawe, P. A. Vermeulen and M. van Drongelen, *Colloid Polym. Sci.*, 2015, **293**, 1607–1614.
35 A. J. Lovinger, *J. Polym. Sci., Polym. Phys. Ed.*, 1980, **18**, 793–809.
36 C. Xing, M. Zhao, L. Zhao, J. You, X. Cao and Y. Li, *Polym. Chem.*, 2013, **4**, 5726–5734.
37 B. S. Morra and R. S. Stein, *J. Polym. Sci., Polym. Phys. Ed.*, 1982, **20**, 2243–2259.
38 X.-Z. Chen, X. Li, X.-S. Qian, S. Wu, S.-G. Lu, H.-M. Gu, M. Lin, Q.-D. Shen and Q. M. Zhang, *Polymer*, 2013, **54**, 2373–2381.
39 H. M. Bao, J. F. Song, J. Zhang, Q. D. Shen, C. Z. Yang and Q. M. Zhang, *Macromolecules*, 2007, **40**, 2371–2379.
40 J. Wang, Z. L. Li, R. A. Pérez, A. J. Müller, B. Zhang, S. M. Grayson and W. B. Hu, *Polymer*, 2015, **63**, 34–40.